

Received: 03 May 2023 / Accepted: 25 May 2023 / Published online: 28 May 2023

*compliant mechanism, multi-objective optimization,
Six Sigma, NSGA-II*

Huy-Tuan PHAM^{1*}, Van-Khien NGUYEN^{1,2},
Quang-Khoa DANG¹, Thi Van Anh DUONG¹,
Duc-Thong NGUYEN³, Thanh-Vu PHAN¹

DESIGN OPTIMIZATION OF COMPLIANT MECHANISMS FOR VIBRATION ASSISTED MACHINING APPLICATIONS USING A HYBRID SIX SIGMA, RSM-FEM, AND NSGA-II APPROACH

Vibration-assisted machining, a hybrid processing method, has been gaining considerable interest recently due to its advantages, such as increasing material removal rate, enhancing surface quality, reducing cutting forces and tool wear, improving tool life, or minimizing burr formation. Special equipment must be designed to integrate the additional vibration energy into the traditional system to exploit those spectacular characteristics. This paper proposes the design of a new 2-DOF high-precision compliant positioning mechanism using an optimization process combining the response surface method, finite element method, and Six Sigma analysis into a multi-objective genetic algorithm. The TOPSIS method is also used to select the best solution from the Pareto solution set. The optimum design was fabricated to assess its performance in a vibration-assisted milling experiment concerning surface roughness criteria. The results demonstrate significant enhancement in both the manufacturing criteria of surface quality and the design approach criteria since it eliminates modelling errors associated with analytical approaches during the synthesis and analysis of compliant mechanisms.

1. INTRODUCTION

Machining technology that simultaneously combines two or more energy sources to achieve superior results compared to using only one type of energy is called hybrid machining. Available technologies in this field include abrasive-water jets, electrochemical discharge, laser, and vibration-assisted machining (VAM) [1]. Recent research in the VAM integrates vibration energy into conventional or non-conventional mechanical manufacturing processes such as turning [2], drilling [3], milling [4], EDM [5], or additive manufacturing [6]. The vibration-integrated source used in these systems is further classified into resonant and non-resonant modes. While in the former method, the vibration frequency can be as high as tens of kilohertz in the ultrasonic range, and it only works at a fixed frequency, the latter works well with a broader range of lower frequencies, typically just below the first resonant

¹ Faculty of Mechanical Engineering, Ho Chi Minh City University of Technology and Education, Vietnam

² Faculty of Mechanical Engineering, Nam Sai Gon Polytechnic College, Vietnam

³ Faculty of Natural Sciences Teacher Education, Dong Thap University, Vietnam

* E-mail: phtuan@hcmute.edu.vn

<http://doi.org/10.36897/jme/166500>

frequency of the system [7]. In subtractive machining methods, the benefits of VAMs could be increased material removal rate, enhanced surface quality, reduced cutting forces, reduced tool wear, improved tool life, enhanced chip evacuation, or minimized burr formation for processing hard and brittle materials [8].

Non-resonant VAMs often require a small and exact motion to oscillate the system. Despite the advantages of the extra vibration embedded into the VAM processes, it must maintain the accuracy of the fabricated parts. Compliant mechanisms (CMs) are structures that use the flexibility of materials to transmit forces and motions without relying on traditional joints or hinges. During the last decades, they have been extensively investigated to substitute the conventional rigid mechanisms since they offer several benefits, including simplicity, fewer parts, precision, weight reduction, improved performance, and versatility [9]. They have been widely used in various applications, such as biomedical engineering [10, 11], high-precision flow control valves [12, 13], energy harvesting mechanisms [14], feed drive mechanisms [15], and equipment for VAMs. Piezoelectric actuators (PZTs) that could offer extremely precise displacement at tens of microns combined with CMs to transfer and amplify the original motion is a popular way to design non-resonant VAM equipment. Researchers often use multiple methods to create CMs that meet their design expectations. These methods can be classified into three categories. The first category is mathematical modelling and analytical analysis, which uses classical mechanical equations to describe the models [16, 17]. The second category is direct optimization design approaches, which extensively utilize genetic algorithm (GA) [15, 18], differential evolution [19], ant colony optimization, and particle swarm optimization [20]. The third and final category is indirect design-of-experiment (DOE) based optimization methods. They use Taguchi, Response surface methodology (RSM) [21], or hybrid approaches such as RSM-GA [22], Taguchi-GA [23], Neural Network-GA [24], and adaptive neuro-fuzzy inference system (ANFIS) [25]. Additionally, the six-sigma reliability analysis can be used to evaluate the design quality in engineering [26–28]. This method has not been commonly used in designing CMs due to the complexity of calculating and predicting their response functions.

All the above design methods have their pros and cons. The mathematical model-based optimization method can quickly solve problems, the direct optimization is suitable for complicated designs and hard-to-build mathematical models, and the DOE-based design methods can save computation time. However, the common limitation of these methods is that they are not interested in evaluating the feasibility of the objective functions and the design variables to improve the reliability and convergence of the design problem. This paper proposes an optimization method combining Six Sigma, RSM-FEM, and NSGA-II to design a CM applied in vibration-assisted milling (VAMill) to improve the surface roughness of the product.

2. DESIGN

2.1. DESIGN CONCEPT

This paper aims to develop a vibration-assisted system and apply it in the milling processing method to exploit the distinct characteristics of this hybrid machining. There are

two strategies to build this system. Ultrasonic-assisted milling or resonant-based VAM usually incorporates the vibration source directly into the milling tool [7]. In contrast, the counterpart non-resonant method integrates it into a platform to vibrate the workpiece. Figure 1 shows a conceptual design of a two-degree-of-freedom CM that can be independently or simultaneously vibrated by two PZT actuators from two perpendicular directions.

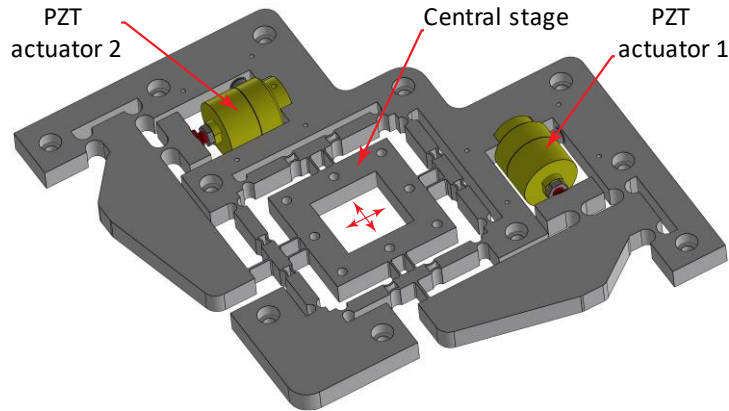


Fig. 1. Conceptual design

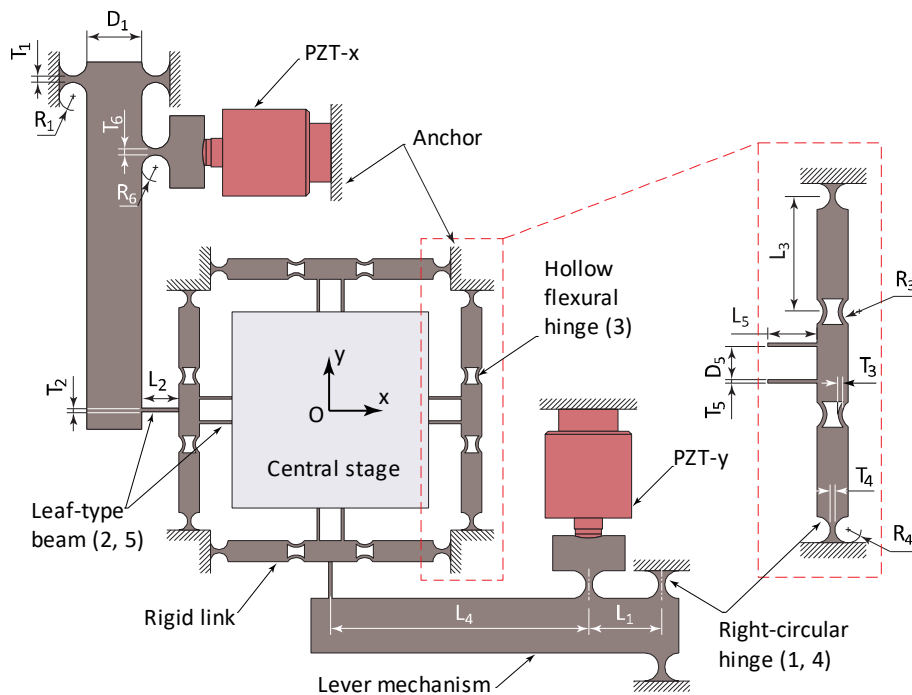


Fig. 2. Design parameters of a high-precision positioning compliant mechanism for vibration-assisted machining

Figure 2 illustrates detailed components of the displacement transmission chain. This CM consists of three types of flexure hinges, including right-circular hinge (1), leaf spring (2), and hollow flexure hinge (3). Between the elastic members are the rigid segments whose dimensions are sufficiently large to resist deformation. Therefore, all flexure hinges shall experience large deformation to fulfil the function of the mechanism. In this design, two lever

mechanisms amplify the precise motion of the PZT actuators. Since the vibration amplitude of the workpiece is relatively small, typically at the micron level, the CM is the ideal option for this purpose.

2.2. PROBLEM FORMULATION

The design process of a CM usually starts with the simplification of the mechanism into a pseudo-rigid-body model (PRBM), where the flexure hinges can be modelled as torsional springs and rigid links [9]. PRBM models of three types of flexure hinge in this paper are illustrated in Fig. 3. The vibration stage in this paper has a parallel configuration in which each direction (x and y) is independently activated. Analysis of one direction is sufficient for the whole design due to its symmetry. Figure 4 converts the 2-DOF mechanism in the x –direction of Fig. 2 into its equivalent PRBM for the analytical analysis in the following sections.

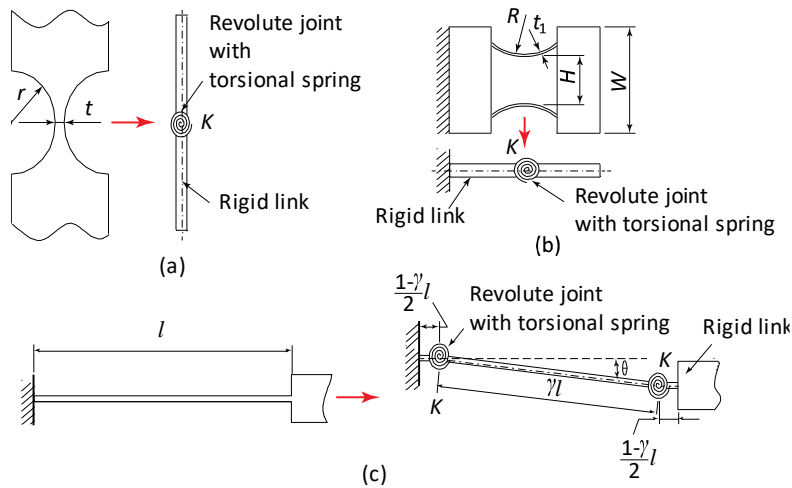


Fig. 3. Pseudo-rigid-body model of a right-circular flexure hinge (a), a hollow flexural hinge (b), and a leaf-type flexure beam (c)

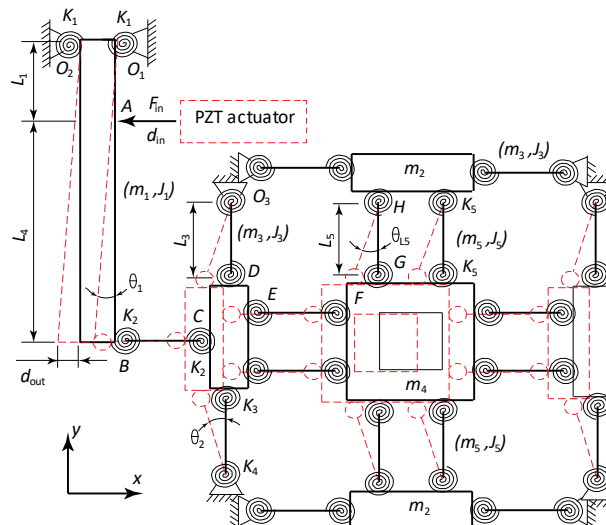


Fig. 4. A pseudo-rigid-body modelling diagram of the vibration-integrated compliant platform

2.2.1. AMPLIFICATION ANALYSIS

In Fig. 4, d_{in} and d_{out} are the input and output displacement of the PZT actuator and the lever mechanism, respectively. Since the lower end of the lever mechanism is attached directly to the central vibration stage via a leaf spring (2) that is always impacted by tensile force, the final vibration amplitude of the workpiece is also equal to d_{out} . It is convenient to establish the displacement equation from this simple geometric relation.

$$d_{out} - \frac{(L_1 + L_4)}{L_1} d_{in} = 0 \quad (1)$$

Suppose that the displacement amplification is regarded as A_{amp} which is defined as the ratio between the output displacement and the input driving motion, it can be calculated as:

$$A_{amp} = \frac{d_{out}}{d_{in}} = \frac{L_1 + L_4}{L_1} \quad (2)$$

2.2.2. DYNAMIC ANALYSIS

VAM applications mainly rely on the vibration of the equipment to exploit its hybrid machining features. Therefore, understanding the dynamic properties of the mechanism is crucial to any processing paradigm. The PRBM diagram in Figure 4 models the mass, length, and angular rotation of the rigid links as m_i, L_i ($i = 1, 2, \dots, 5$) and θ_i ($i = 1, 2$), respectively. The equivalent torsional spring constant of the circular hinges (K_1, K_4) as a result of converting them into PRBM, as shown in Fig. 3(a), is presented in Equation (3). The moment of inertia of each rigid link (J_i) is calculated in Equations (4) [29].

$$K_i = \frac{2Eb_iT_i^{5/2}}{9\pi R_i^{1/2}}, \quad (i = 1, 4) \quad (3)$$

$$J_i = \frac{m_i L_i^2}{12} \quad (4)$$

where the dimensions of the elastic circular hinge, including the radius, the out-of-plane and minimum in-plane thickness, are illustrated as R_i, b_i , and T_i , respectively; E is the Young's modulus of the material.

The equivalent torsional stiffness (K_5) and the cross-sectional area moment of inertia (I_5) of the leaf-type beams are calculated using Equations (5a) and (5b) [29].

$$K_5 = 2\gamma K_{\theta 5} \frac{EI_5}{L_5} \quad (5a)$$

$$I_5 = \frac{b_5 h_5^3}{12} \quad (5b)$$

where L_5 , b_5 , and h_5 are the length, in-plane and out-of-plane thickness of the leaf-type beams; other empirical parameters due to the modelling conversion, $K_{\theta_5} = 2.65$, $\gamma = 0.85$, are the stiffness coefficient and characteristic radius factor, respectively [9]

The rotation angle (θ_{L_5}) of a leaf-type beam modelling in Fig. 3(c) and denoting in Fig. 4 is calculated in the following Equation (6).

$$\theta_{L_5} = \frac{d_{out}}{\gamma L_5} = \frac{A_{amp}}{\gamma L_5} d_{in} \quad (6)$$

The equivalent torsional stiffness (K_3) and the cross-sectional area moment of inertia (I_3) of the hollow flexural hinge 3 are calculated in Equations (7a) and (7b) [29]:

$$K_3 = \rho K_{\theta_3} \frac{EI_3}{l} \quad (7a)$$

$$I_3 = \frac{b_3 h_3^3}{12} \quad (7b)$$

where l , b_3 , and h_3 are the length, in-plane and out-of-plane thickness of the curved beam of the hollow flexural hinges; other empirical parameters, $K_{\theta_3} = 2.99$, $\rho = 0.794$, are referenced to [9].

Suppose that the PZT actuator applies an input force F_{in} to the rigid lever beam at point A, a work (W) done by this force is calculated as Equation (8):

$$W = \frac{1}{2} F_{in} d_{in} \quad (8)$$

Neglecting the segments without deformation, the remaining parts will store the elastic energy V_p , as shown in Equation (9), within its body as a distinct property of the CM. In some special types of the CM, this amount of energy can be harvested to use for that specific purpose.

$$\begin{aligned} V_p &= \frac{1}{2} (2K_1) \theta_1^2 + 4 \left[\frac{1}{2} (2K_3) \theta_2^2 + \frac{1}{2} K_4 \theta_2^2 + \frac{1}{2} (2K_5) \theta_{L_5}^2 \right] \\ &= \frac{1}{2} \left[2K_1 + 8 \left(\frac{L_1 + L_4}{L_3} \right)^2 K_3 + 4 \left(\frac{L_1 + L_4}{L_3} \right)^2 K_4 + 8 \left(\frac{A_{amp} L_1}{\gamma L_5} \right)^2 K_5 \right] \theta_1^2 \end{aligned} \quad (9)$$

Using the principle of virtual work $W = V_p$, we obtain the Equation (10):

$$\frac{1}{2} F_{in} d_{in} = \frac{1}{2} \left[\frac{2K_1}{L_1^2} + 8 \left(\frac{L_1 + L_4}{L_1 L_3} \right)^2 K_3 + 4 \left(\frac{L_1 + L_4}{L_1 L_3} \right)^2 K_4 + 8 \left(\frac{A_{amp}}{\gamma L_5} \right)^2 K_5 \right] d_{in}^2 \quad (10)$$

where θ_j is the rotation angle of the rigid links. The system of Equations (11) describes the relation between θ_j and d_{in} :

$$\begin{cases} \theta_1 = \frac{d_{in}}{L_1} \\ \theta_2 = \frac{(L_1 + L_4)}{L_3} \theta_1 = \frac{(L_1 + L_4)}{L_1 L_3} d_{in} \end{cases} \quad (11)$$

From Equation (10), it is easy to calculate the stiffness K_{in} of the 2-DOF mechanism:

$$K_{in} = \frac{2K_1}{L_1^2} + 8 \left(\frac{L_1 + L_4}{L_1 L_3} \right)^2 K_3 + 4 \left(\frac{L_1 + L_4}{L_1 L_3} \right)^2 K_4 + 8 \left(\frac{A_{amp}}{\gamma L_5} \right)^2 K_5 \quad (12)$$

Besides the strain energy, the oscillating structure also gains kinetic energy due to the translation and angular motions of different components, as shown in Equation (13):

$$T_K = \sum_{i=1}^5 (TE_i + RE_i) = \sum_{i=1}^5 \left(\frac{1}{2} m_i v_i^2 + \frac{1}{2} J_i \dot{\theta}_i^2 \right) \quad (13)$$

Cascading the Equation (13) for each rigid link, we obtain Equation (14)

$$\begin{aligned} T_K = & \frac{1}{2} m_1 (L_1 \dot{\theta}_1)^2 + \frac{J_1 \dot{\theta}_1^2}{2} + m_2 (A_{amp} L_1 \dot{\theta}_1)^2 + 2m_3 (A_{amp} L_1 \dot{\theta}_1)^2 \\ & + 2J_3 \left(\frac{L_1 + L_4}{L_3} \dot{\theta}_1 \right)^2 + \frac{1}{2} m_4 (A_{amp} L_1 \dot{\theta}_1)^2 + 2m_5 (A_{amp} L_1 \dot{\theta}_1)^2 \\ & + 2J_5 \left(\frac{A_{amp} L_1}{\gamma L_5} \dot{\theta}_1 \right)^2 + \frac{1}{2} \left(\frac{1 - \gamma}{2} \right) 4m_5 (A_{amp} L_1 \dot{\theta}_1)^2 \end{aligned} \quad (14)$$

Using the Lagrangian method with $\Gamma = T_K - V_p$

$$\frac{d}{dt} \left(\frac{\partial \Gamma}{\partial \dot{\theta}_1} \right) - \frac{\partial \Gamma}{\partial \theta_1} = Q_1 \quad (15)$$

$$\bar{J} \ddot{\theta}_1 + \bar{K} \theta_1 = 0 \quad (16a)$$

where:

$$\begin{aligned} \bar{J} = & m_1 L_1^2 + J_1 + 2m_2 (A_{amp} L_1)^2 + 4m_3 (A_{amp} L_1)^2 + 4J_3 \left(\frac{L_1 + L_4}{L_3} \right)^2 \\ & + m_4 (A_{amp} L_1)^2 + 4m_5 (A_{amp} L_1)^2 + 4J_5 \left(\frac{A_{amp} L_1}{\gamma L_5} \right)^2 \end{aligned} \quad (16b)$$

$$\begin{aligned} \bar{K} = & 2K_1 + 8 \left(\frac{L_1 + L_4}{L_3} \right)^2 K_3 + 4 \left(\frac{L_1 + L_4}{L_3} \right)^2 K_4 + 8 \left(\frac{A_{amp} L_1}{\gamma L_5} \right)^2 K_5 \end{aligned} \quad (16c)$$

Equation (16a) is a second-order differential equation without damping effect and it can be used to investigate the dynamic behaviour of the motion of the flexural beams. The natural frequency ω_0 can be determined using Equation (17)

$$\omega_0 = \sqrt{\frac{\bar{K}}{\bar{J}}} \quad (17)$$

3. OPTIMIZATION DESIGN

Generally, the compliant platform analysed in Section 2 has two degree-of-freedom (DOFs) that would facilitate the hybrid vibration-assisted micro-milling process in this research. Its design is a complex task that requires careful consideration of several factors. One critical aspect is the need to achieve a precisely designed dynamical behaviour that can withstand alternating stress for an extended period. Moreover, the structural responses of the designed CM also involve large nonlinear deformations, making it a multi-objective design problem. Overall, this design problem has three objective functions, including:

1. Maximize the first natural frequency.
2. Minimize the parasitic motion or the coupling effect between the two DOFs.
3. Minimize the concentrated stress.

Therefore, developing the mechanism requires an appropriate optimization design process to meet these intricate expectations. To tackle this complex design task, this research proposes a hybrid optimization method combining Six Sigma and the well-known Non-dominated Sorting Genetic Algorithm (NSGA-II). The hybrid approach leverages the strengths of both optimization techniques to improve the efficiency and effectiveness of the design process. This algorithm is illustrated in Fig. 5.

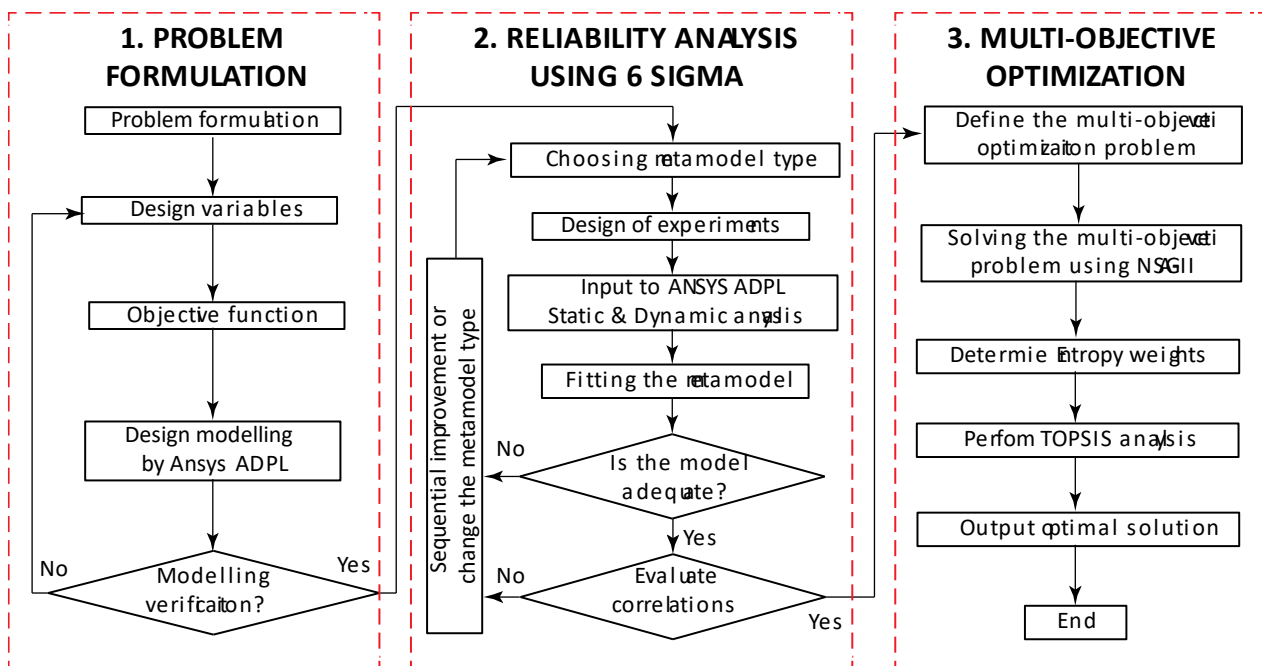


Fig. 5. The hybrid optimization using Six sigma and NSGA-II algorithm

The hybrid optimization algorithm in Fig. 5 undergoes three steps.

Step 1: Problem define and formulation.

Design modelling using Ansys ADPL; define design variables (DVs), constraint functions, and objective functions; Convergence analysis to verify the initial model.

Step 2: Reliability analysis using Six Sigma.

Choose the metamodel type and design of experiments;

Implement static and dynamic analysis using finite element method (FEM), find the regression models by response surface methodology (RSM) and artificial neural network (ANN);

Check the adequacy of the models;

Analyse the DVs and evaluate the objective functions using the Six Sigma method. This step aims to explore the main effect of the DVs and their interaction. It also eliminates less significant DVs and chooses the most feasible objective functions.

Step 3: Multi-objective optimization.

Define the multi-objective optimization problem;

Solve the problem using NSGA-II;

Choose the best alternative from the Pareto front using the Technique for Order of Preference by Similarity to Ideal Solution (TOPSIS). TOPSIS is a multi-criteria decision-making method that involves the calculation of the relative closeness of each alternative to the positive ideal solution based on their distance in a multi-dimensional space [30–32]. The Entropy weight derived from the probability theory in the TOPSIS mitigates the subjective effects that one can encounter in other methods, such as Analytical Hierarchical Process (AHP) or Delphi [33].

3.1. RELIABILITY ANALYSIS USING SIX SIGMA

The mechanism in Fig. 2 utilizes three types of flexural hinges to synthesize the equipment. Right-circular hinges 1, 4, and 6 are parameterized using the radius and minimum in-plane thickness as (R_1, T_1) , (R_4, T_4) , and (R_6, T_6) , respectively. The DVs for the leaf-type beams 2 and 5, including (L_2, T_2) and (L_5, T_5) , are their length and in-plane thickness, respectively. Finally, the hollow flexural hinge 3 uses the radius and beam thickness (R_3, T_3) as DVs. For the dimensions of the rigid links, L_1 and L_4 are the arm's length of the lever mechanism, and L_3 is the distance between the centers of the right-circular hinge 4 and the hollow hinge 3. The displacement amplification ratio of the lever mechanism determined by equation (2) is chosen as $A_{amp} = 1.5$ for simplicity. These DVs confine the dimensions of the central stage. The minimum width of the lever mechanism and the distance between two leaf-type beams 5 denoting D_1 and D_5 , respectively, are predetermined to ensure the rigidity of the structure. Consequently, only the dimensions of the flexural hinges are chosen as twelve DVs for the optimization problem, including (R_1, T_1) , (L_2, T_2) , (R_3, T_3) , (R_4, T_4) , (L_5, T_5) , and (R_6, T_6) .

Before implementing the proposed design optimization process, conducting a DV sensitivity analysis is crucial to understand the influence of each variable on the objective functions and to determine which ones have the most significant impact on the design. This step can reduce the design space and optimize the design process to converge toward the best solution. Moreover, by understanding the sensitivity of the DVs, designers can set realistic constraints on them to ensure the design meets the required performance specifications. Thus, it enhances the convergence speed of the optimization algorithm and reduces the processing time.

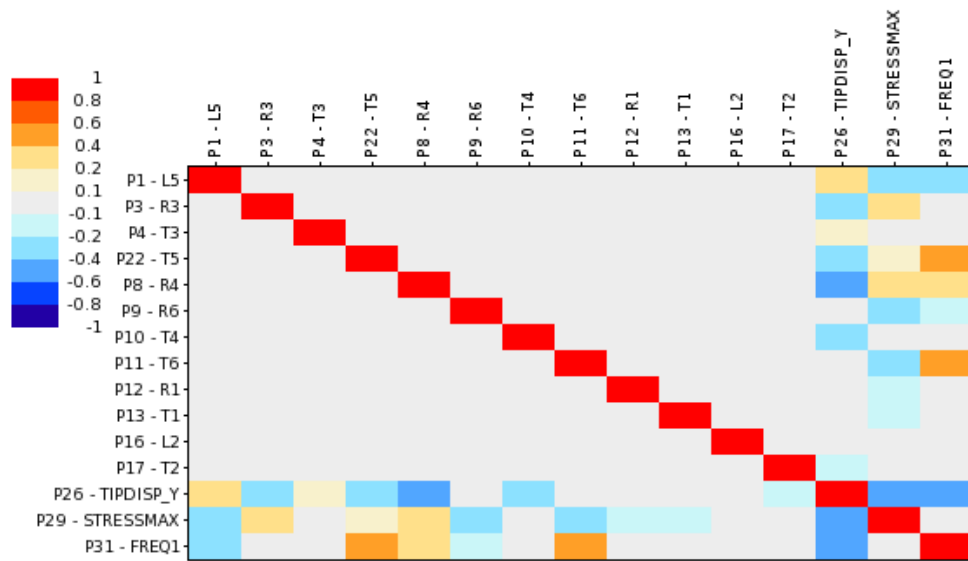


Fig. 6. The correlation matrix of design variables

Figures 6 and 7 illustrate the sensitivity analysis results of the twelve DVs on three objective functions, including the unexpected parasitic motion (P26–TIPDISP_Y), the equivalent maximum stress (P29–STRESSMAX), and the first natural frequency (P31–FREQ1). In Fig. 7, since the objective of the parasitic motion (P26) is minimization, the negative but expected impact DVs to this output are R_4 , T_6 , R_6 , L_5 , R_3 , R_1 , T_5 , T_4 , T_1 , and T_2 with a decreasing order, respectively. The leaf-beam length L_2 and the hollow-hinge thickness T_3 tend to increase the output P26 when they are increased. With the maximum stress output P29, the DVs R_4 , T_6 , L_5 , R_6 , R_1 , T_4 , R_3 , T_5 , and T_2 would induce large stress concentration within the hinges; meanwhile, the DVs T_3 , L_2 , and T_1 would attenuate it. Figure 7 also shows that the DVs R_4 , T_6 , R_6 , L_5 , R_3 , R_1 , T_5 , T_4 , T_1 , L_2 , and T_2 positively impact the natural frequency output parameter P31. However, the effect of the hollow-hinge thickness T_3 is disproportionate to this objective function.

In the reliability analysis, the randomized design of experiments is generated and evaluated using FEM. The three output responses are then regressed, and these models are predicted using the combination of RSM and ANN in ANSYS. Figure 8 illustrates the predicted model verification from the observed design points. The distribution of the design points on the diagonal lines in this figure represents the accuracy of these models. It is clearly seen that they are linearly arranged for all three objective functions, including the first-mode natural frequency, the stress, and the parasitic motion. However, variability exists in any practical system. Therefore, validation experiments will then evaluate the prediction accuracy of the proposed method.

Before taking the necessary statistical analysis to evaluate the reliability of the mechanism, the DV sensitivity analysis to the output responses has shown promising results. Next, the Six Sigma analysis for the three output responses is implemented, and their results are illustrated in Fig. 9. The probability density distribution for the first-mode natural frequency, parasitic motion, and maximum stress in Fig. 9(a, b, c) shows a normal distribution with a familiar bell shape. This result confirms the high reliability of the statistical analysis model.

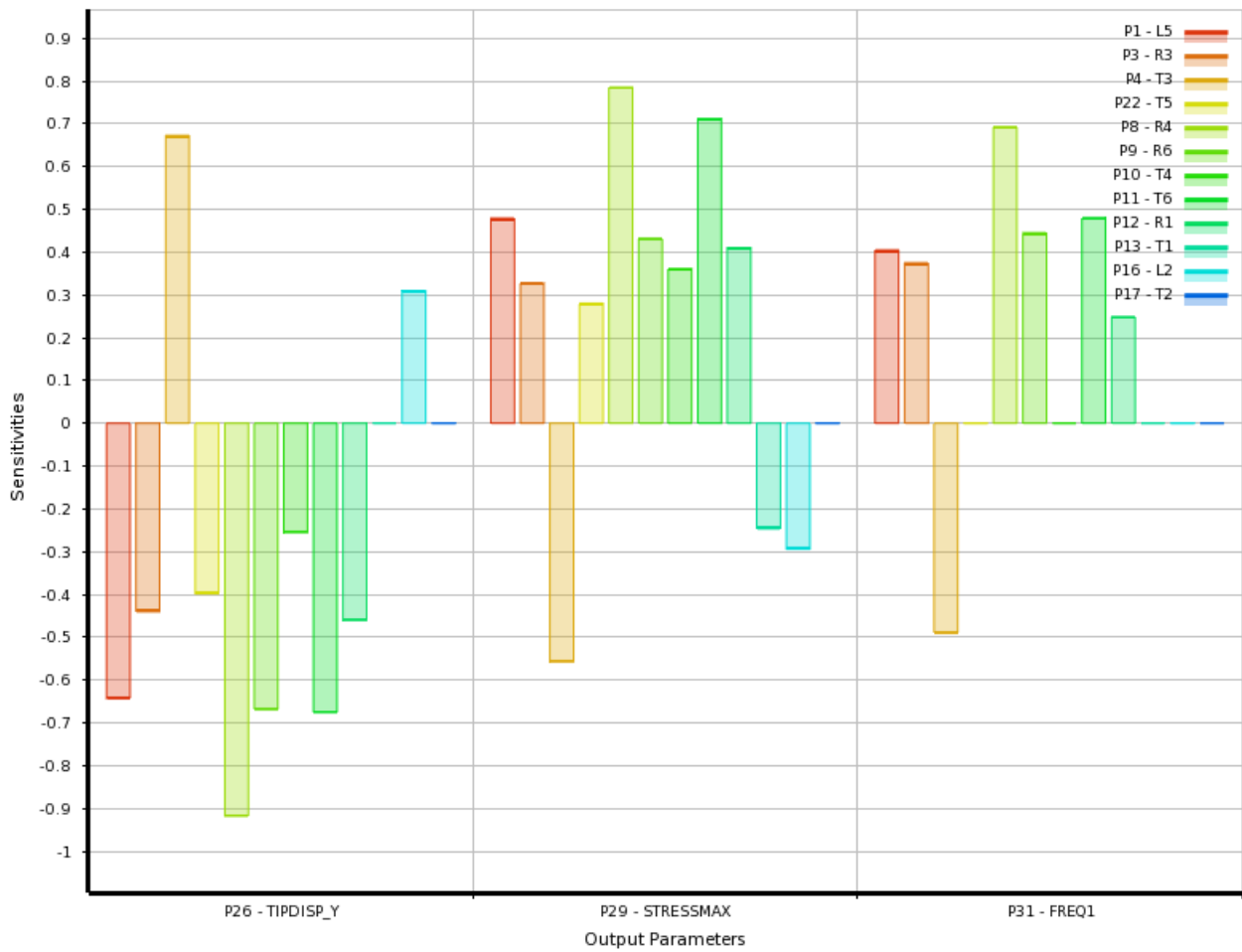


Fig. 7. DV sensitivity analysis to the objective functions

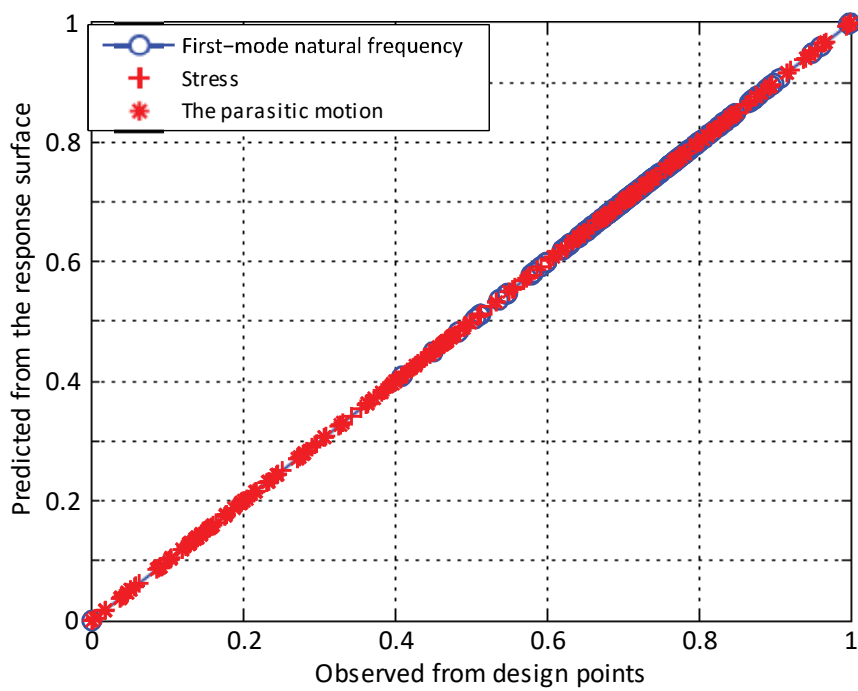
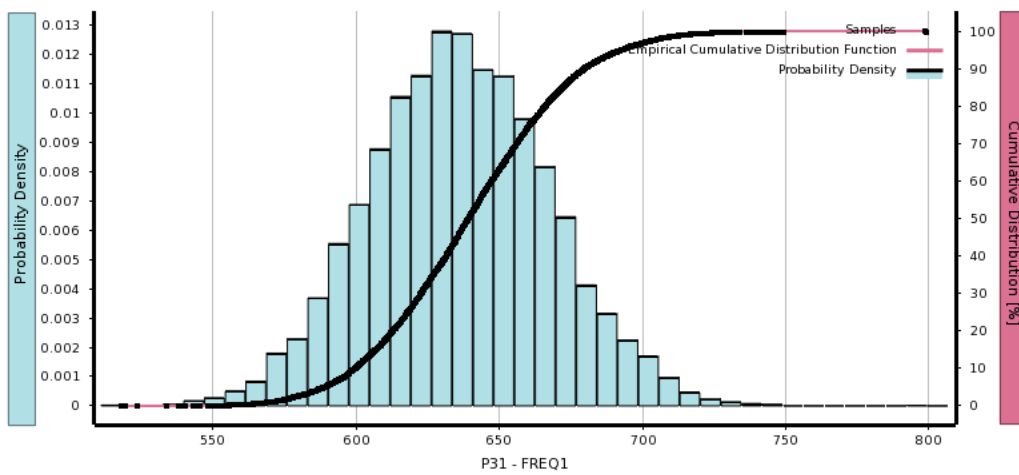
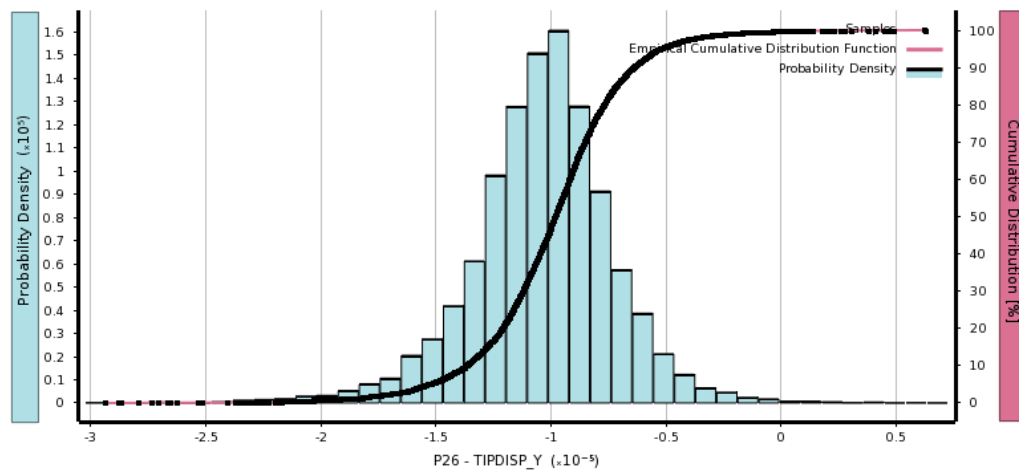


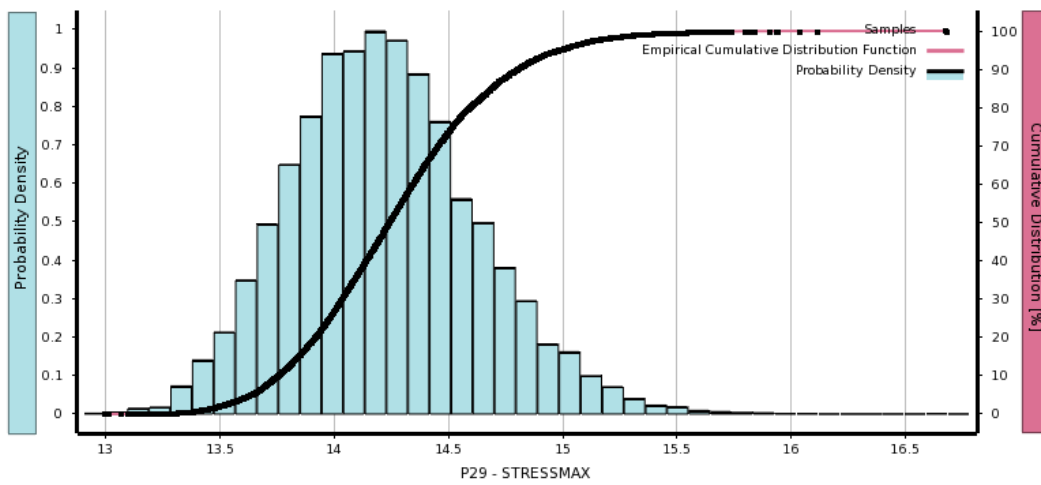
Fig. 8. Response surface regression model evaluation



(a)



(b)



(c)

Fig. 9. Statistical analysis results for the output responses: (a) the first-mode natural frequency; (b) parasitic motion; (c) maximum stress

3.2. COMPLIANT MECHANISM OPTIMIZATION USING NSGA-II

Considering the allowable design space when the device is assembled, the realistic processing conditions, and the available PZT actuators, the constraints of the DVs and the objective functions of the problem are formulated in Table 1. Three objective functions are described in Equations (18–20). The boundary of the DVs is described in Equations (21–24). For the best operation of the PZT actuators, the manufacturer recommends the operating range following Equation (25). Although the simple geometrical analysis in Equation (2) has predetermined the displacement amplification $A_{amp} = 1.5$, the practical deformation of the CM still relies on the flexibility of the compliant hinges. Equation (26) imposes a constraint g_6 to prevent the amplification ratio from diminishing below the expected value. In summary, this optimization design problem in Table 1 has three objective functions, twelve DVs, and eight constraint functions.

Table 1. Optimization design formulation of the problem

1. Objective functions:	
$f_1 = \text{Maximize}(f_0)$	(18)
$f_2 = \text{Minimize}(\delta_y)$	(19)
$f_3 = \text{Minimize}(\sigma_m)$	(20)
2. Design variables:	
Right circular hinges: $T_1, R_1, T_4, R_4, T_6, R_6$.	
Leaf-type beams: T_2, L_2, T_5, L_5 .	
Hollow flexural hinges: T_3, R_3 .	
3. Constraint functions:	
i. (g_1): $1.0 \leq T_1, T_2, T_3, T_4, T_5 \leq 3.0$, (mm)	(21)
ii. (g_2): $3.0 \leq T_6 \leq 6.0$, (mm)	(22)
iii. (g_3): $12 \leq L_2, L_5 \leq 20$, (mm)	(23)
iv. (g_4): $3.0 \leq R_1, R_3, R_4, R_6 \leq 6.0$, (mm)	(24)
v. (g_5): $K_{in} \leq 0.2K_{pzt}$	(25)
vi. (g_6): $\frac{D_{out}}{D_{in}} > 1.5$	(26)
vii. (g_7): Overall dimensions = 340 x 340 mm ² .	(27)
viii. (g_8): $\sigma_m < [\sigma_y]/SF$	(28)

To find a feasible design for the CM applied in VAMill, a shape and size hybrid optimization process, as described in Fig. 5, is used. The DV sensitivity analysis and the NSGA-II are implemented using the ANSYS Mechanical ADPL. The Pareto front from the NSGA-II results will be further analysed using TOPSIS to find the best solution for the current application.

Figure 10 describes the Pareto front from the NSGA-II results. The goal of this research is to maximize the objective function f_1 (the first-mode natural frequency) and simultaneously minimize the objective function f_2 (the parasitic motion) and the objective function f_3 (concentration stress). However, when a candidate in Fig. 10 has a high natural frequency, its maximum stress and parasitic motion are also elevated. This dilemma situation hampers the selection of the best solution since the objective functions are in conflict. When each objective function is independently considered, many possible combinations exist for choosing a solution. Therefore, the TOPSIS method is used to assist decision-making.

Considering the diversity and uncertainty among the criteria, the Entropy weight approach reduces the likelihood of instability and inconsistency in the weights and the ranking of alternatives. After implementing this TOPSIS analysis, potential candidates are figured out. Their comparison and estimation to find the best design are presented in Table 2.

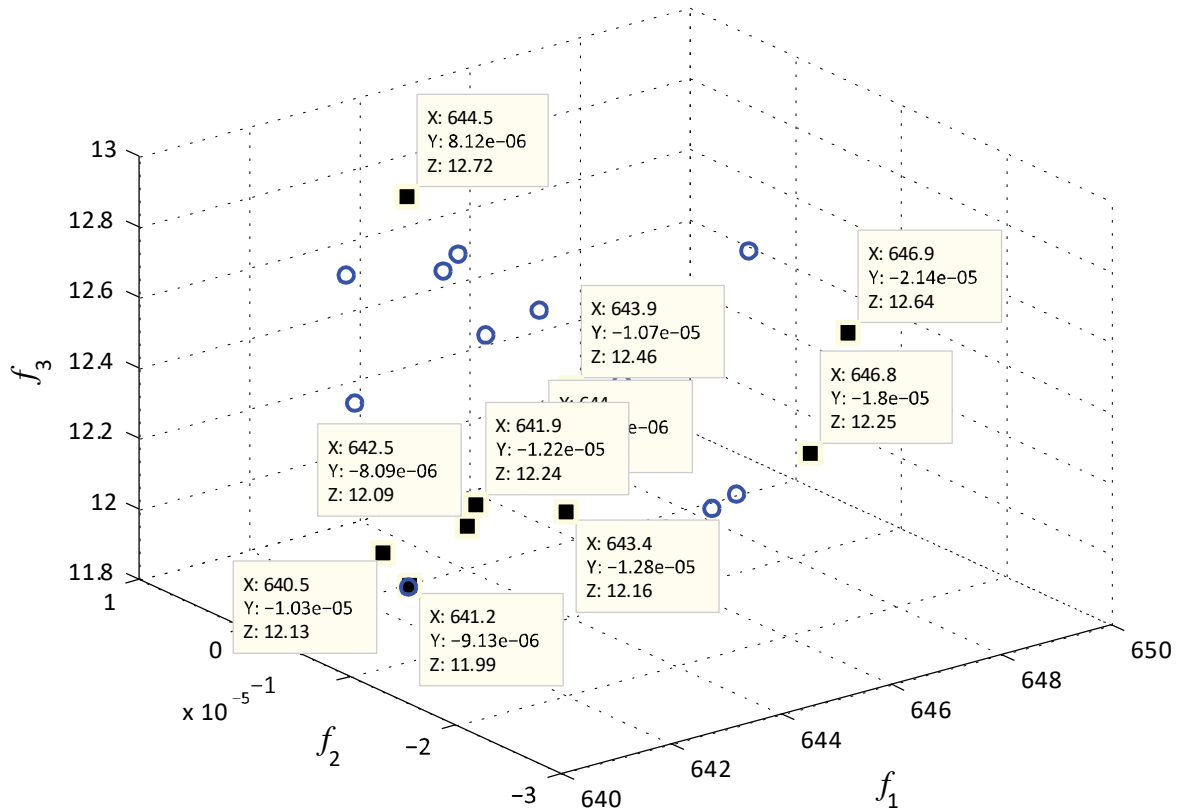


Fig. 10. The Pareto front of the NSGA-II results

Table 2. The TOPSIS ranking results of candidates

No	f_1 (Hz)	f_2 (μm)	f_3 (MPa)	Score	Ranking
375	641.249	-9.13E-06	11.993	0.9429	1
388	645.388	-1.18E-05	12.015	0.9196	2
389	640.524	-1.28E-05	12.068	0.8649	3
347	642.501	-8.09E-06	12.093	0.8388	4
254	645.464	-1.58E-05	12.124	0.8064	5

Using the TOPSIS ranking methods, five feasible candidates have been selected and presented in Table 2. The design number 375 on the top row of the table has the highest score. By comparing with the randomly generated designs in the initial population of the NSGA-II algorithm, the natural frequency of the optimum candidate has improved 38%, and the maximum stress has been reduced by 27%. These encouraging results verify the benefits of implementing the proposed optimization process. Specific dimensions of the chosen optimum solution are described in Table 3.

Table 3. Optimal solutions.

Design variables	Value (mm)	Objective functions	Value
R_1	5.09	f_1 (mode 1)	641.2 (Hz)
T_1	1.96	f_2	0 (μm)
T_2	1.41	f_3	11.99 (MPa)
L_2	13.64	f_1 (mode 2)	642.1 (Hz)
R_3	4.84		
T_3	1.11		
R_4	3.73		
T_4	1.21		
T_5	1.56		
L_5	17.15		
R_6	5.69		
T_6	3.87		

3.3. RESULTS ANALYSIS AND DISCUSSIONS

ANSYS R18.2 is used to simulate the displacement along the x and y directions, the equivalent stress distribution, and modal analysis of the optimum design in Table 3. A FEM model is built to evaluate the performance of the mechanism before its prototype fabrication. 2D plane strain element PLANE183 is chosen to analyse and simulate the design problem. This analysis uses aluminum alloy (Al 7075–T6) as the fabricated material. Its properties are described in Table 4. Aluminum Al 7075-T6 is a widely used high-strength alloy known for its excellent strength-to-weight ratio. However, it exhibits anisotropic behaviour, meaning its mechanical properties may vary with direction. The 2-DOF vibration stage design is assumed to have symmetrical behaviour in both directions. Therefore, practical verification must be done in both directions when it is fabricated to evaluate the anisotropic effect. The simulation results are illustrated in Fig. 11. With the input displacement $D_{in} = 4 \mu\text{m}$, provided in the x -direction, the output motion D_{out} of the central stage is $7.484 \mu\text{m}$, as shown in Fig. 11(a). This displacement equals the amplification $A_{amp} = 1.871$. The parasitic motion in the y -direction (δ_y) is negligible in Fig. 11(b). The maximum concentrated stress of the mechanism in Fig. 11(c), $\sigma_{max} = 12.53 \text{ MPa}$, is relatively small compared to the yield strength of the fabricated material. For the modal analysis, the first two modes, $f_{01} = 641.2 \text{ Hz}$ and $f_{02} = 642.1 \text{ Hz}$, are the first-mode natural frequency of the mechanism when it is vibrated in the x and y directions, respectively. They are shown in Fig. 11(d) and 11(e).

Table 4. Mechanical properties of Al 7075–T6

Mechanical property	Symbol	Value	Unit
Young's modulus	E	71.7	GPa
Poisson's ratio	ν	0.33	
Yield strength	σ_y	503	MPa
Density	ρ	2810	kg/m^3

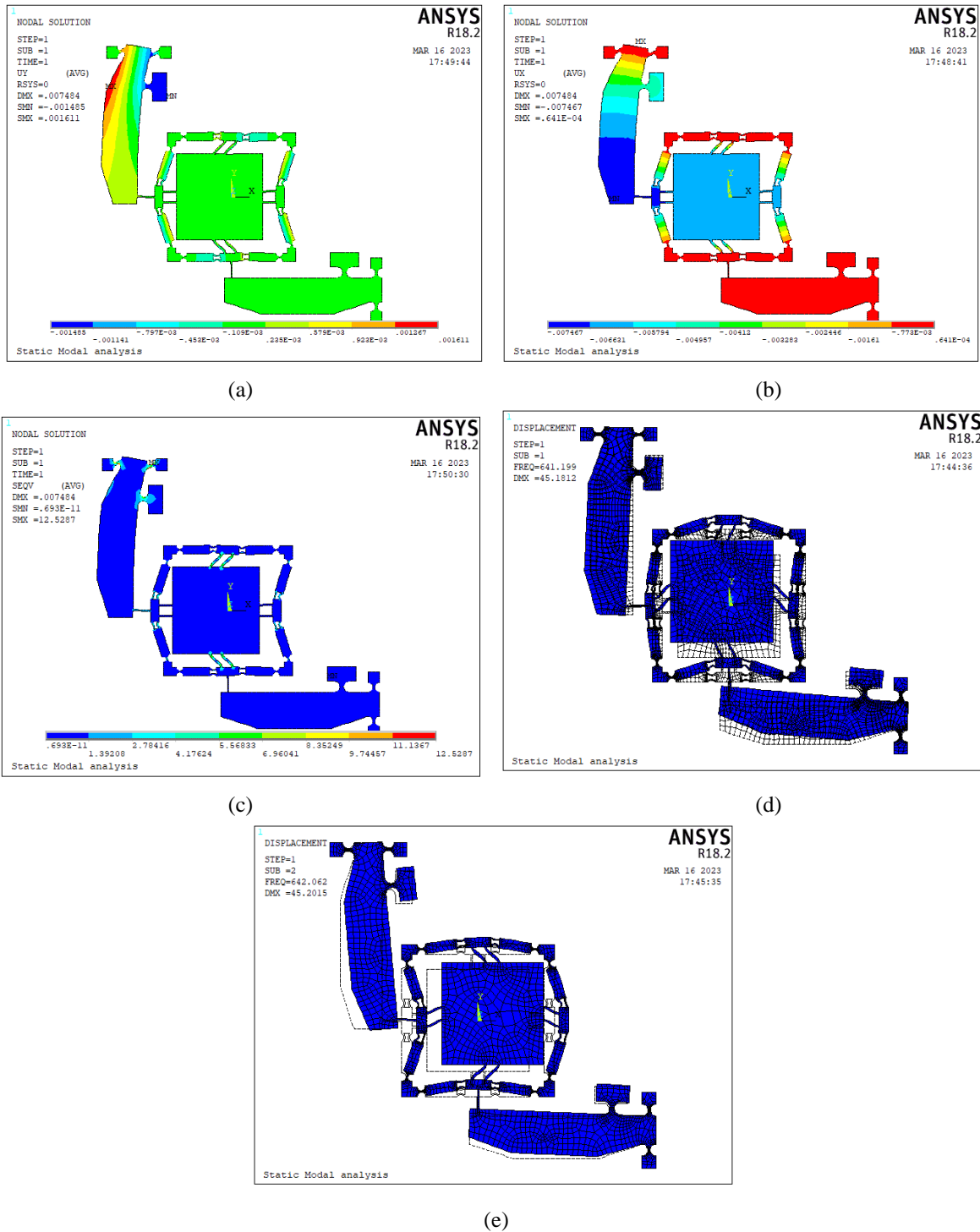


Fig. 11. Simulation results of the optimum design: (a) displacement in the x-direction, (b) the parasitic motion δ_y , (c) equivalent stress distribution, (d, e) first-mode natural frequencies

Figure 12 shows the simulation and experimental natural frequency of the chosen optimum design. While the first two modes of the FEM are $f_{01} = 641.2$ Hz and $f_{02} = 642.1$ Hz, the measured results in Fig. 12(b) are $f_{01}^E = 689$ Hz and $f_{02}^E = 692.7$ Hz. The dynamic behaviours of the device calculated by different methods, including analytical, simulation, and experiment, are summarized in Table 5. Supposing that the experimental data

is used as a standard, the error of the analytical results is smaller than 3.3%, and this error of the simulation results is less than 7.5%. The discrepancy among these methods originates from the difference in the final fabricated dimensions of the flexural hinges. Since the fabricated device will be used in a non-resonant VAM, the realized natural frequencies are not exactly required to match the resonant frequency of the PZT actuators as in the case of resonant VAM. The only requirement of the natural frequency for the designed mechanism is as large as possible. This characteristic of non-resonant VAM makes it easier for the engineer to design the equipment.

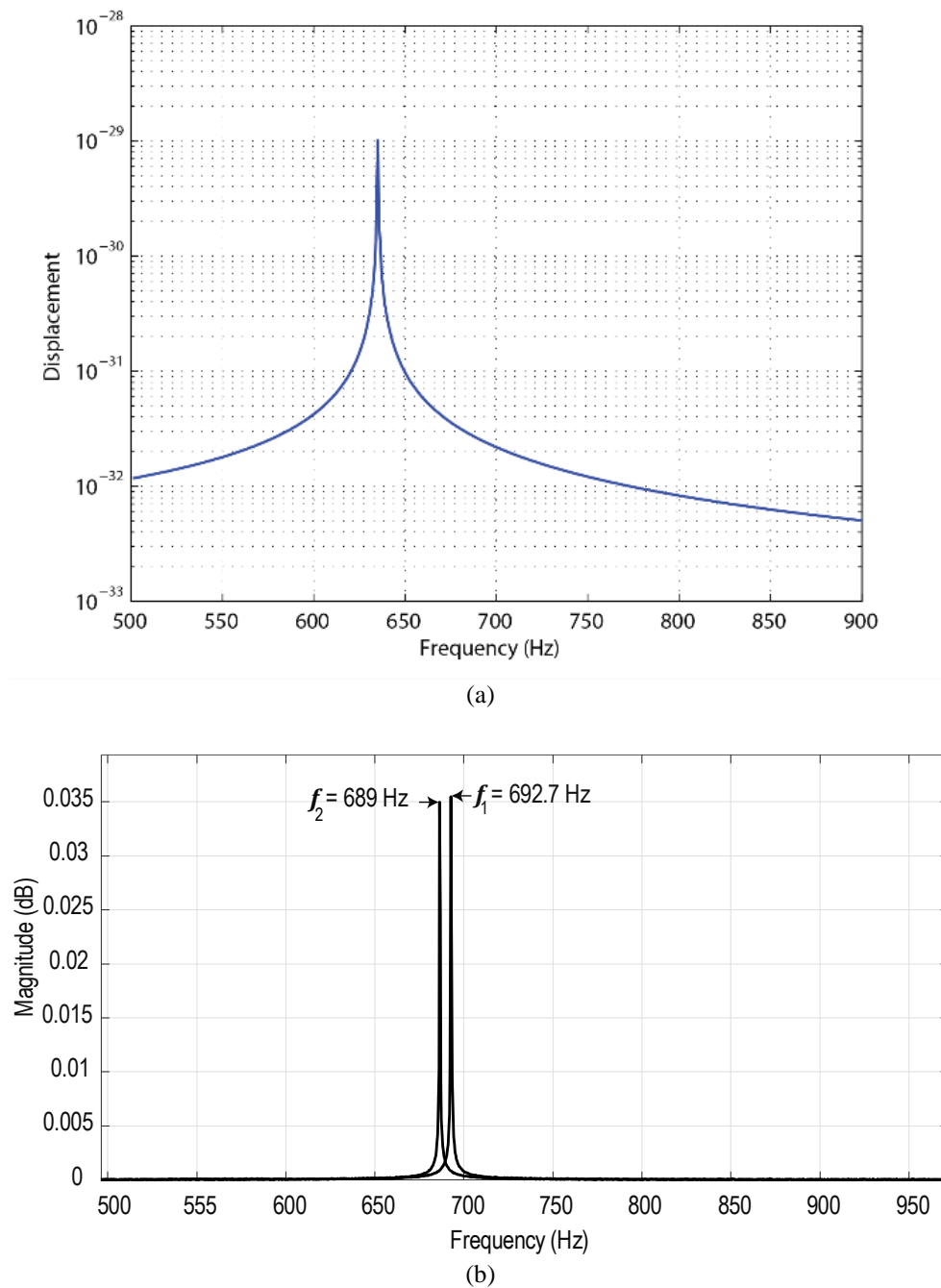


Fig. 12. The first-mode natural frequency results using (a) simulation method; (b) experimental measurement

Table 5. Analytical, simulation vs. experiment results in comparison

Dynamic behaviours	Experiment	Simulation/ Error (%)	Analytical/ Error (%)
Natural frequency mode 1 (Hz)	692.7	641.2 (7.43%)	711.2 (2.67%)
Natural frequency mode 2 (Hz)	689	642.1 (6.81%)	711.2 (3.22%)

Table 6: Previous research benchmarking

Studies	Natural frequency (Hz)	Parasitic motion (μm)	Stress (MPa)
Li [34]	66.79	1.04	64.54
Syahputra [35]	211	2.06	Unknown
Gu [36], Chen [37]	220.43	Unknown	102.98
Lai [38]	181.29	Unknown	207.61
Gu [39]	411.23	Unknown	33.07
This study	692.7	0	12.53

Table 6 compares the overall performance of the designed mechanism, including the first-mode natural frequency, maximum stress, and parasitic motion, with several previous studies. The comparison shows that the current design possesses a relatively high first-mode natural frequency, comparatively low maximum concentrated stress, and negligible parasitic motion. These characteristics are favorable for the majority of the VAM applications

4. EXPERIMENT

4.1. NATURAL FREQUENCY EVALUATION

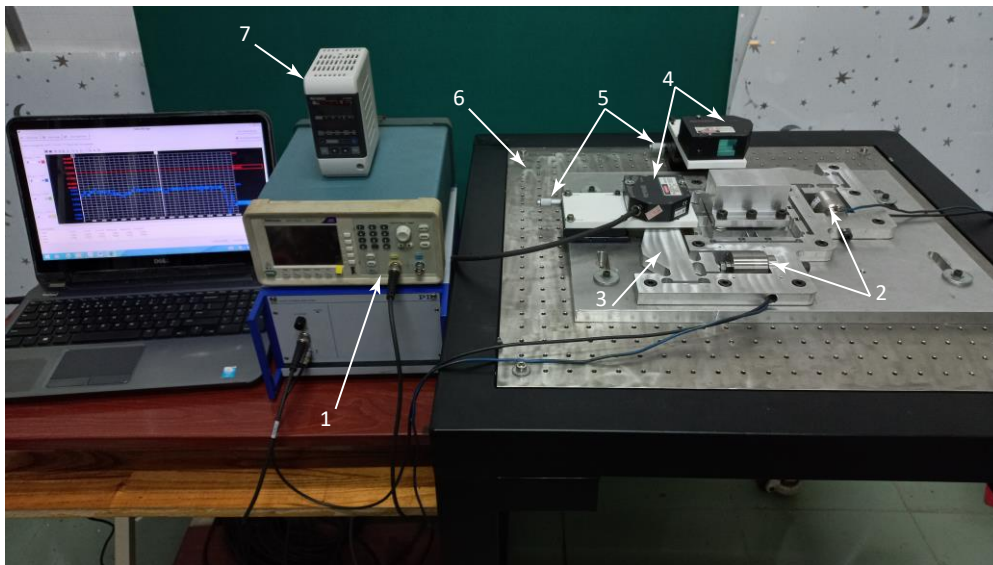


Fig. 13. Experimental setup to measure the displacement and natural frequency: (1) function generator; (2) PZT actuators; (3) 2-DOF positioning mechanism; (4) displacement laser sensor; (5) micro-translation stage; (6) vibration-isolated table; (7) laser sensor controller

An experimental setup is arranged as shown in Fig. 13 to evaluate the theoretical and simulation calculation results of the dynamic performance of the mechanism. Natural frequency is measured by providing a sinusoidal waveform signal from a function generator AFG1022 (Tektronix Inc., USA) to two PZT actuators P-225.10 (Physik Instrumente PI, Germany). The vibration of the central stage in two directions (x and y) is captured by the high-speed, high-accuracy CCD laser displacement sensor LK-G30 (Keyence Corporation, Japan), with a resolution of $0.05\ \mu\text{m}$. When the PZT actuator in the x -direction is activated, the x -axis laser sensor detects the displacement in the intended direction. Meanwhile, the y -axis laser sensor will record the unexpected parasitic motion in the other direction and vice versa. The measured data is analysed using the fast Fourier transform (FFT), and its result is presented in Fig. 12b. The first peak of the frequency spectrum is at $692.7\ \text{Hz}$.

4.2. PRACTICAL VAMILL REALIZATION

The slot milling experiments of VAMill are established, as shown in Fig. 14, to quickly evaluate the performance of the new hybrid machining method compared to the traditional milling process. The experiment uses the CNC milling machine VMC-650 (Huey

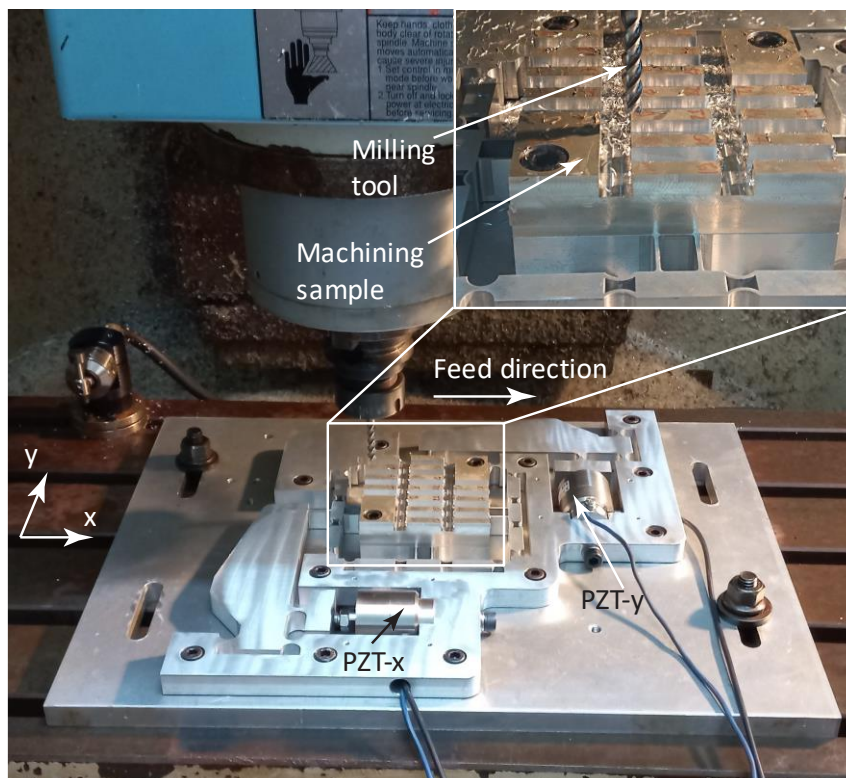


Fig. 14. Vibration-assisted milling experiment setup

Long, Taiwan) to implement the cuttings. The sample material is aluminum Al-6061. The VAMill equipment has two DOFs that allow the sample to vibrate in two directions

separately or simultaneously, namely along the feed direction (x -direction) and the perpendicular direction (y -direction). Currently, this experiment only examines the effect of vibration in the feed direction. Therefore, two vibration factors are considered, including the vibration frequency f_{VAM} and amplitude a_{VAM} , to explore the impact of the vibration energy integrated into the machining process. The amplitude has two levels (0 and $3 \mu\text{m}$), and the vibration frequency is tested with six levels (0, 75, 175, 325, 650, and 700 Hz). In this experiment, a solid carbide square endmill tool with a diameter of 6 mm was used. This scanning experiment does not consider the effect of other machining technological parameters, such as spindle speed (S), feed rate (F), and the cutting tool properties, and their interaction effects. Instead, they are preliminarily chosen as $S = 3000 \text{ rpm}$ and $F = 200 \text{ mm/min}$. All information for the experimental machining process is summarized in Table 7.

Table 7. Experimental machining conditions

Parameters	Values	Parameters	Values
Milling machine	VMC-650	Spindle speed	3000 rpm
Workpiece material	Al-6061	Feed rate	200 mm/min
Tool material	Solid carbide	Depth of cut	0.2 mm
Tool diameter	6 mm	Vibration direction	Feed direction
Flutes	3	Vibration frequencies	0, 75, 175, 325, 650, and 700 Hz
Lubrication method	Dry milling	Vibration amplitude	0; $3 \mu\text{m}$
Cutting length	25 mm		

The output criteria to evaluate the machining performance in this experiment is the surface roughness R_a . Fig. 15 illustrates the surface roughness measurement setup. The surface tester SJ-210 (Mitutoyo, Japan) was used to measure each machining slot. The measurement results for each experimental run are summarized in Table 8.

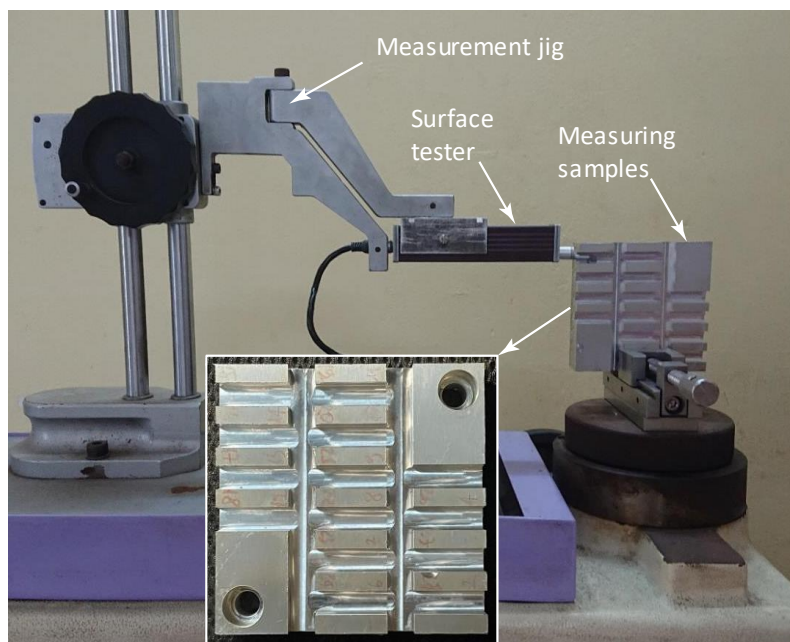


Fig. 15. Surface roughness measurement setup

Table 8. VAMill experiment runs

No.	Vibration amplitude (μm)	Frequency (Hz)	Surface roughness, Ra (μm)		
			Left (1)	Right (2)	Bottom (3)
1	0	0	2.78	3.92	1.7
2	3	75	1.72	1.98	1.56
3	3	175	1.61	1.82	1.71
4	3	325	1.13	1.96	1.38
5	3	650	1.65	2.47	1.75
6	3	700	1.37	2.15	1.67

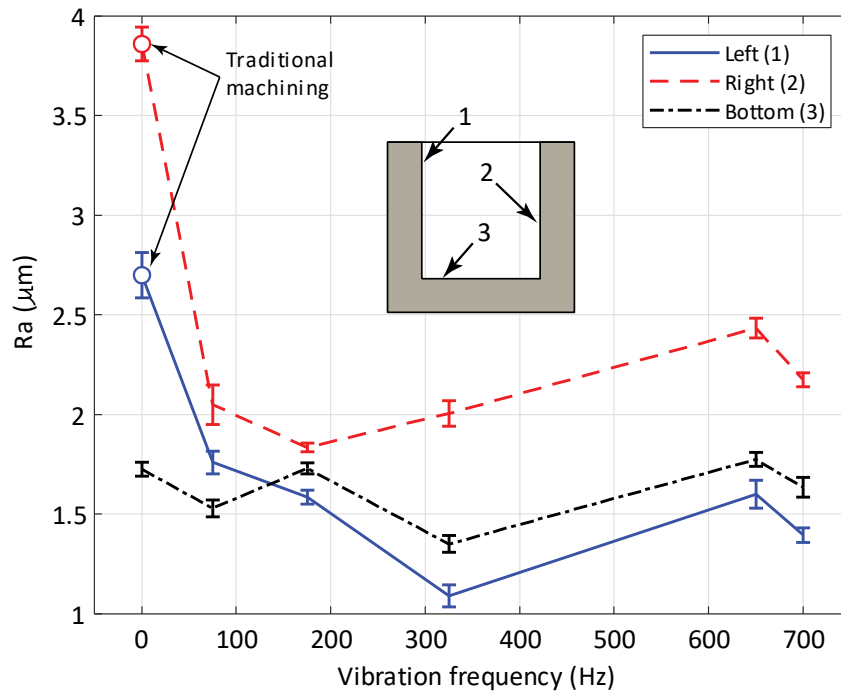


Fig. 16. Surface roughness measurement results

Although the verification machining experiment has two factors, the experimental run with $f_{VAM} = 0 \text{ Hz}$ and $a_{VAM} = 0 \mu\text{m}$ is the traditional milling without vibration. This experiment can be considered a single-factor design since the vibration amplitude $a_{VAM} = 3 \mu\text{m}$ is fixed for other runs. In order to analyse the variance of the experiment, each frequency level is replicated twice. Therefore, twelve experimental runs are randomly implemented to mitigate any nuisance factors due to the machine or the machining process. The effect of the vibration frequency on the machining surface roughness can be observed in Fig. 16. For each milling slot of the machining sample, surface roughness is measured on three surfaces, namely left (1), right (2), and bottom (3). Each surface is measured three times. The mean and standard deviation of each level are presented in Fig. 16. This graph exhibits a discontinuous course for frequency increment because when we want to maintain the vibration amplitude at a constant level of $3 \mu\text{m}$, both frequency and supplied voltage have to be changed simultaneously. It is a try-and-error effort to locate the frequency to provide the expected vibration amplitude. From Fig. 16, the runs with integrated vibration show better quality for two side surfaces compared to traditional machining. This vibration factor does not have an apparent effect on the bottom surface. The general trend for the surface roughness

improvement shows that the roughness of surfaces (1) and (2) is enhanced when the vibration frequency is increased from 0 Hz to less than 325 Hz. However, when the frequency is further increased, it worsens. The bottom surface (3) does not improve when the frequency varies within the investigated range. It is too early to conclude which frequency range would enhance the roughness when the interaction between the vibration factors and other machining technological parameters has not been thoroughly investigated in a specific experimental strategy. A comprehensive research exploring the main and interaction effects between different factors in a VAMill application using the optimum designed mechanism will be discussed and presented in other research.

5. CONCLUSION

This research presents a novel high-precision 2-DOF positioning stage design for vibration-assisted milling. It was optimized using a hybrid approach that combines Six Sigma, RSM-FEM, NSGA-II, and TOPSIS. Through analytical, simulation, and experiment evaluations, the static and dynamic performance of the prototype were validated, showing a maximum discrepancy of less than 7.43% across different calculation methods. A machining experiment was also implemented to demonstrate the advantages of VAMill over traditional milling processes, specifically in terms of surface roughness criteria. A single-factor machining experiment varying vibration frequency from 0 to 700 Hz indicated an improvement in surface roughness when the frequency was below 325 Hz. However, the surface quality decreased when the frequency was further increased. These findings provide an encouraging basis for further investigation and realization of VAMill applications in practical settings. Future research should focus on conducting a comprehensive study that considers the main effects of machining and vibration factors and their interactions. By thoroughly examining these factors, the true potential and applicability of VAMill can be fully understood and harnessed to enhance manufacturing efficiency in working with hard and brittle materials.

ACKNOWLEDGEMENTS

This research was supported by the Ho Chi Minh City University of Technology and Education, project grant number B2021-SPK-02, funded by the Ministry of Education and Training, and hosted by the Ho Chi Minh City University of Technology and Education, Vietnam.

REFERENCES

- [1] BHATTACHARYYA B., DOLOI B., 2019, *Modern Machining Technology: Advanced, Hybrid, Micro Machining and Super Finishing Technology*, Academic Press.
- [2] KIEN H.T., DANG Q.H., PHAM H.T., et al., 2021, *Theoretical and Experimental Study of Vibration-Assisted Turning*, Proceedings of the 2nd Annual International Conference on Material, Machines and Methods for Sustainable Development (MMMS2020), 37–44, Springer, https://doi.org/10.1007/978-3-030-69610-8_5.

- [3] ERFANI A., GHANDEHARIUN A., AFSHARFARD A., 2022, *Experimental Investigation and Optimization of Low-Frequency Vibration-Assisted Drilling*, The International Journal of Advanced Manufacturing Technology, 123/9, 3171–3182.
- [4] ZHENG L., CHEN W., HUO D., 2019, *Experimental Investigation on Burr Formation in Vibration-Assisted Micro-Milling of Ti-6Al-4V*, Proceedings of the Institution of Mechanical Engineers, Part C, Journal of Mechanical Engineering Science, 233/12, 4112–4119.
- [5] PHAN N.H., MUTHURAMALINGAM T., TRONG LY N., VAN DUA T., 2022, *Effect of Ultrasonic Low-Frequency Vibration and its Direction on Machinability in WEDM Process*, Materials and Manufacturing Processes, 37/9, 1045–1051.
- [6] IJEN S., 2020, *Ultrasonic Assisted Fused Deposition Modeling to Improve Mechanical Properties of Recycled Acrylonitrile Butadiene Styrene*, Materials Science, Corpus ID: 221795535.
- [7] CHEN W., HUO D., SHI Y., HALE J., 2018, *State-of-the-Art Review on Vibration-Assisted Milling: Principle, System Design, and Application*, The International Journal of Advanced Manufacturing Technology, 97, 2033–2049.
- [8] BREHL D.A. DOW T., 2008, *Review of Vibration-Assisted Machining*, Precision Engineering, 32/3, 153–172.
- [9] HOWELL LARRY L., 2001, *Compliant Mechanisms*, Ed. John Wiley and Sons, New York.
- [10] PHAM H.T., NGUYEN V., MAI V., 2014, *Shape Optimization and Fabrication of a Parametric Curved-Segment Prosthetic Foot for Amputee*, Journal of Science & Technologies: Technical Universities, 102, 89–95.
- [11] PHAM H.T., LE M.N., MAI V.T., 2016, *A Novel Multi-Axis Compliant Prosthetic Ankle Foot to Support the Rehabilitation of Amputees*, 3rd International Conference on Green Technology and Sustainable Development (GTSD), IEEE, 238–243.
- [12] LING M., HE X., WU M., CAO L., 2022, *Dynamic Design of a Novel High-Speed Piezoelectric Flow Control Valve Based on Compliant Mechanism*, IEEE/ASME Transactions on Mechatronics, 27/6, 4942–4950.
- [13] LING M., WANG J., WU M., CAO L., FU B., 2021, *Design and Modeling of an Improved Bridge-Type Compliant Mechanism with its Application for Hydraulic Piezo-Valves*, Sensors and Actuators A: Physical, 324, 112687.
- [14] NGO T.H., CHI I.T., CHAU M.Q., WANG D.A., 2022, *An Energy Harvester Based on a Bistable Origami Mechanism*, International Journal of Precision Engineering and Manufacturing, 23/2., 213–226.
- [15] NGUYEN V.K., PHAM H.T., PHAM H.H., DANG Q.K., 2021, *Optimization Design of a Compliant Linear Guide for High-Precision Feed Drive Mechanisms*, Mechanism and Machine Theory, 165, 104442.
- [16] LI H. et al., 2022, *Design and Modeling of a Compact Compliant Stroke Amplification Mechanism with Completely Distributed Compliance for Ground-Mounted Actuators*, Mechanism and Machine Theory, 167, 104566.
- [17] WANG F., et al., 2018, *A Novel Actuator-Internal Micro/Nano Positioning Stage with an Arch-Shape Bridge-Type Amplifier*, IEEE Transactions on Industrial Electronics, 66/12, 9161–9172.
- [18] PHAM H.T., WANG D.-A., 2011, *A Constant-Force Bistable Mechanism for Force Regulation and Overload Protection*, Mechanism and Machine Theory, 46/7, 899–909.
- [19] TORREALBA R.R. UDELMAN S.B., 2016, *Design of Cam Shape for Maximum Stiffness Variability on a Novel Compliant Actuator Using Differential Evolution*, Mechanism and Machine Theory, 95, 114–124.
- [20] KAMEL O.M., et al., 2020, *A Novel Hybrid ant Colony-Particle Swarm Optimization Techniques Based Tuning STATCOM for Grid Code Compliance*, IEEE Access, 8, 41566–41587.
- [21] WU J., JIANG Z., WAN L., SONG H., ABBASS K., 2021, *Robust Optimization for Precision Product Using Taguchi-RSM and Desirability Function*, Arabian Journal for Science and Engineering, 46, 2803–2814.
- [22] HUANG S.C. DAO T.P., 2016, *Design and Computational Optimization of a Flexure-Based XY Positioning Platform Using FEA-Based Response Surface Methodology*, International Journal of Precision Engineering and Manufacturing, 17, 1035–1048.
- [23] NGUYEN V.K., PHAM H.T., PHAM H.H., 2017, *Optimal Design of High Precision Compliant Guide Mechanism Using Gene Algorithm and Taguchi-Based Sensitivity Analysis*, International Conference on System Science and Engineering (ICSSE), IEEE, 412–417.
- [24] YE T. LI Y., 2023, *Synthesis of 2-dof Decoupled Rotation Stage with Fea-Based Neural Network*, Processes, 11/1, 192.
- [25] BAYAT S., PISHKENARI H.N., SALARIEH H., 2019, *Observer Design for a Nano-Positioning System Using Neural, fuzzy and ANFIS networks*, Mechatronics, 59, 10–24.
- [26] KOCH P., 2002, *Probabilistic Design: Optimizing for Six Sigma Quality*, 43rd AIAA/ASME/ASCE/AHS/ASC Structures, Structural Dynamics, and Materials Conference, 1471.
- [27] CHEN D., WANG Y., LIU R., ZHANG J., QIU L., 2021, *Reliability Analysis of the Optimized Carrying Door Frame Based on Six-Sigma*, Journal of Physics, Conference Series, IOP Publishing, 1948/1, 012125.
- [28] NGUYEN T.T., et al., 2021, *Reliability Analysis of Concrete-Filled Steel Tube Columns Under Axial Compression*, AIP Conference Proceedings, AIP Publishing, LLC 2406/1, 060017.
- [29] PAROS J.M., 1965, *How to Design Exural Hinges*, Mach. Design., 37, 151–156.

- [30] HWANG C.-L.A., MASUD S.M., 2012, *Multiple Objective Decision Making—Methods and Applications: A State-of-the-art Survey*, Springer Science & Business Media.
- [31] CALIŞKAN H., et al., 2013, *Material Selection for the Tool Holder Working Under Hard Milling Conditions Using Different Multi Criteria Decision Making Methods*, *Materials & Design*, 45, 473–479.
- [32] OLSON D., 2004, *Comparison of Weights in TOPSIS Models*, *Mathematical and Computer Modelling*, 40/7–8, 721–727.
- [33] KUMAR J., VERMA R.K., 2020, *Experimental Investigations and Multiple Criteria Optimization During Milling of Graphene Oxide (GO) Doped Epoxy/CFRP Composites Using TOPSIS-AHP Hybrid Module*, *FME Transactions*, 48/3, 628–635.
- [34] LI Y., WU Z., ZHAO X., 2013, *Optimal Design and Control Strategy of a Novel 2-DOF Micromanipulator*, *International Journal of Advanced Robotic Systems*, 10/3, 162.
- [35] SYAHPUTRA H.P., KO T.J., CHUNG B.M., 2014, *Development of 2-Axis Hybrid Positioning System for Precision Contouring on Micro-Milling Operation*, *Journal of Mechanical Science and Technology*, 28, 691–697.
- [36] GU Y. et al., 2018, *Vibration-Assisted Roll-Type Polishing System Based on Compliant Micro-Motion Stage*, *Micromachines*, 9/10, 499.
- [37] CHEN X., et al., 2020, *Study on Subsurface Damage and Surface Quality of Silicon Carbide Ceramic Induced by a Novel Non-Resonant Vibration-Assisted Roll-Type Polishing*, *Journal of Materials Processing Technology*, 282, 116667.
- [38] LAI W., GAO J., ZHANG L., ZHONG Y., 2020, *Parallel and Decoupled xy Flexible Positioning Platform for Micro Led Panel Repair*, 21st International Conference on Electronic Packaging Technology (ICEPT), IEEE, 1–6.
- [39] GU Y. et al., 2020, *Design, Analysis, and Testing of a Novel 2-DOF Vibration-Assisted Polishing Device Driven by the Piezoelectric Actuators*, *The International Journal of Advanced Manufacturing Technology*, 111, 471–493.